Earthquake Ground-Motion Simulation including Nonlinear Soil Effects under Idealized Conditions with Application to Two Case Studies

Article *in* Seismological Research Letters · November 2012

DOI: 10.1785/0220120079

CITATIONS
40

READS
543

3 authors:

Ricardo Taborda
The University of Memphis
68 PUBLICATIONS **827** CITATIONS
SEE PROFILE

Jacobo Bielak
Carnegie Mellon University
229 PUBLICATIONS **6,753** CITATIONS
SEE PROFILE

Deicy Restrepo
Hogeschool Zuyd
8 PUBLICATIONS **46** CITATIONS
SEE PROFILE

Earthquake Ground-Motion Simulation including Nonlinear Soil Effects under Idealized Conditions with Application to Two Case Studies

by R. Taborda, J. Bielak, and D. Restrepo

INTRODUCTION

Nonlinear soil behavior in sediments remains one of the most relevant and challenging aspects in site characterization. Geotechnical engineers began studying soil changes in the shear modulus and damping ratio with increasing strain amplitude in the late 1960s and early 1970s (e.g., Seed and Idriss, 1969; Hardin and Drnevich, 1972). However, the influence of soil nonlinearities on the ground motion, in places other than those involving liquefaction, was not fully accepted by seismologists until observations made after the 1989 Loma Prieta and 1994 Northridge earthquakes, and from monitoring projects such as the SMART1 and SMART2 arrays in Taiwan (Field *et al.*, 1998; Aki, 2003). These events and arrays showed that soil nonlinearities caused permanent deformations away from the source, reductions in soil-to-rock ratios by average factors of 2 with respect to those of smaller events, and reductions in shear moduli and shear-wave velocities of up to 80% and 50%, respectively (e.g., Wen, 1994; Beresnev *et al.*, 1995; Field *et al.*, 1997). Soil nonlinearities seem to be more prominent in frequency ranges from 0.5 to 4 Hz (e.g., Darragh and Shakal, 1991; Field *et al.*, 1997; Beresnev, 2002), and have been associated with peak ground acceleration values above 0.1–0.2 g and shear strains larger than 10^{-5} to 10^{-4} (e.g., Chang *et al.*, 1989; Chin and Aki, 1991; Beresnev and Wen, 1996; Trifunac and Todorovska, 1996).

Modeling and simulation of nonlinear soil behavior and effects also date back to the 1960s and 1970s (e.g., Idriss and Seed, 1968; Schnabel, Seed, and Lysmer, 1972; Joyner and Chen, 1975). Early 1D and 2D studies were mostly done using equivalent linear models. Although these models do not capture all the characteristics of nonlinear plastic behavior (e.g., Streeter *et al.*, 1974; Finn *et al.*, 1978), they are deeply rooted in engineering practice (Field *et al.*, 1998), and they continue to be used through computer programs such as SHAKE91 (Schnabel, Lysmer, and Seed, 1972; Idriss and Sun, 1993). There exists, on the other hand, an abundance of plastic models used to describe the yielding and cyclic stress-strain behavior of soils (e.g., Dafalias and Popov, 1975; Prévost, 1977, 1985; Dafalias, 1986). These models usually involve a significant number of soil parameters upon which there is no agreement among modelers. In addition, some of them can be computationally demanding. This has hindered their use. Nonlinear soil effects are then often incorporated through 1D analysis, where the incident motion at the interface between the softer sediments and the harder substrata has been previously computed from a linear simulation or obtained from records on rock (e.g., Hartzell *et al.*, 2002; Archuleta *et al.*, 2003; Assimaki *et al.*, 2008). Other options are 2D and 2½D models under incident plane waves (e.g., Zhang and Papageorgiou, 1996; Zhang *et al.*, 2008). Full 3D nonlinear soil simulations, on the other hand, in which every aspect of the analysis is 3D, have been reserved for sensitive infrastructure projects such as bridges, dams, or nuclear power plants, and limited to modeling scales constrained by computational resources (e.g., Vaughan and Isenberg, 1984; Elgamal *et al.*, 2008).

Although these alternatives have yielded reasonable estimates, they have not fully addressed the 3D aspects present in a region where soil nonlinearities are combined with source, path, and basin effects. To our knowledge there have been only a limited number of 3D nonlinear soil simulations, which synthesize the collective contribution of these effects at regional scales (Xu *et al.*, 2003; Dupros *et al.*, 2010; Taborda, 2010). Here, we describe a methodology used for incorporating full 3D nonlinear-soil behavior in large-scale earthquake simulations, and present results obtained for two case studies in realistic basins, under idealized conditions. We model the soil using an explicit rate-dependent approach implemented in a parallel finite-element software. Our main goals are: (1) to test our implementation and (2) to qualitatively evaluate the implications of including nonlinear soil behavior in 3D large-scale earthquake simulations. We analyze the results obtained for the ground motion in two study cases from a local and regional perspective. The simulations yield results that are qualitatively meaningful in consideration of the chosen conditions and observations from past earthquakes, though not necessarily equivalent. We discuss the approach taken and relate ongoing efforts to improve our simulation capabilities.

doi: 10.1785/0220120079

METHODOLOGY

Deterministic earthquake ground-motion simulation entails the solution of a wave propagation problem in a solid medium. Under elastic conditions, this problem can be expressed by Navier's equations of elastodynamics, which can be extended to include the effects of intrinsic attenuation. An abundance of numerical methods exists to solve wave propagation problems in heterogeneous anelastic media. In recent years, finite difference and low- and high-order finite-element (FE) techniques have been particularly useful in large-scale earthquake simulations (e.g., Frankel and Vidale, 1992; Olsen *et al.*, 1995; Faccioli *et al.*, 1997; Graves, 1998; Seriani, 1998; Komatitsch and Vilotte, 1998; Bao *et al.*, 1998; Aagaard *et al.*, 2008; Bielak *et al.*, 2010). Using FE techniques, for instance, one can discretize Navier's equations entirely in terms of displacements. This facilitates the implementation and solution processes considerably.

In the case of nonlinear, elasto-(visco)-plastic materials, however, one needs to preserve the stress tensor throughout the formulation to ensure that the stress-strain relationship complies with the chosen plasticity rule at all times. Using FE techniques, the discrete form of the linear momentum equation can be written as

$$\mathbf{M}\ddot{\mathbf{u}} + \sum_e \int_{\Omega_e} \mathbf{B}^T \sigma d\Omega_e = \mathbf{f}, \tag{1}$$

where $\mathbf{M}$ is the system's mass matrix, $\ddot{\mathbf{u}}$ is the second time derivative of the vector of nodal displacements, $\mathbf{f}$ is the vector of nodal forces, $\mathbf{B}$ is the discretized strain tensor, and σ is the stress tensor written as a vector field. The integral term in equation (1) represents the internal resistance force, and the summation over e means assembly of all elements Ω_e in the FE mesh.

It follows from equation (1) that the solution of the displacement requires evaluating σ for all elements. Within the elastic range, stresses are directly obtained from strains. Once a stress point in any given element reaches the elastic limit or is in plastic deformation or plastic flow, the stress tensor must satisfy the relationship with strains according to a chosen plasticity rule. Plasticity rules are customarily defined based on a yield function, $f(F, k)$, which depends both on the current state of stresses $F = F(\sigma_{ij})$ and on a corresponding yield condition, $k = k(\sigma_{ij}, k_n)$, where k_n represents different yielding and/or hardening parameters that explain the plastic behavior of the material.

According to classical theory of plasticity, the total strain (ϵ) can be expressed as the sum of its elastic (ϵ^e) and plastic (ϵ^p) components,

$$\epsilon_{ij} = \epsilon^e_{ij} + \epsilon^p_{ij}, \tag{2}$$

and therefore,

$$\sigma_{ij} = C_{ijmn}(\epsilon_{mn} - \epsilon^p_{mn}), \tag{3}$$

where C_{ijmn} is the 3D fourth-order elastic constitutive tensor. Because the magnitude of the plastic strain ϵ^p_{ij} is unlimited under plastic flow, the plastic strain is determined in terms of strain increments or strain rates, $\dot{\epsilon}^p_{ij}$. Strain rates are governed by a chosen flow rule and a plastic potential function. The plastic flow equation can be written as

$$\dot{\epsilon}^p_{ij} = \dot{\lambda}\frac{\partial g(\sigma_{ij})}{\partial \sigma_{ij}}. \tag{4}$$

Here, $\dot{\lambda}$ is a positive scalar factor of proportionality for the plastic strain rate, commonly known as the plastic multiplier, and $g(\sigma_{ij})$ is a scalar function that defines the plastic potential. In the special case when the plastic potential coincides with the yield function, that is, when $g(\sigma_{ij}) = f(\sigma_{ij})$, the flow rule is said to be associated. In this study, we adopt an associated flow rule.

Notice that equation (3) requires one to know the contribution of the plastic deformation to the total strain. This marks a difference in the way one approaches equation (4). On the one hand, in rate-independent plasticity, the plastic multiplier $\dot{\lambda}$ is unknown. Therefore, the plastic strain is customarily obtained by solving a succession of elasticity problems for which a formulation or path is provided. This often requires iterative procedures to guarantee that strains and stresses are compatible with the chosen yield function. On the other hand, in rate-dependent plasticity, following Perzyna (1963, 1966), the plastic multiplier can be expressed as

$$\dot{\lambda} = \dot{\lambda}_0 \left\langle \frac{F(\sigma_{ij})}{k(\sigma_{ij}, k_n)} \right\rangle^{\frac{1}{m}}, \tag{5}$$

and therefore the change in plastic strain can be directly predicted from the current state of plastic strain, that is, $\epsilon^p_{n+1} = \epsilon^p_n + \Delta t \dot{\epsilon}^p$. Here, $\dot{\lambda}_0$ and m are the material's strain-rate scaling and sensitivity factors, respectively; the operator $\langle\cdot\rangle$ is such that $\langle\Theta\rangle \neq 0$ only if $\Theta > 0$. For the case of an associated flow rule, equation (4) becomes

$$\dot{\epsilon}^p_{ij} = \dot{\lambda}_0 \left\langle \frac{F(\sigma_{ij})}{k(\sigma_{ij}, k_n)} \right\rangle^{\frac{1}{m}} \frac{\partial f(\sigma_{ij})}{\partial \sigma_{ij}}. \tag{6}$$

Rate-dependent plasticity is particularly suitable for problems involving viscosity and creep. For most geomaterials, with the exception of rocks under high pressure, the effects of viscosity and creep are usually neglected. Therefore, soils in geotechnical applications have been usually modeled using rate-independent methods. It can be proved, however, that in the limit (as $m \to 0$), the rate-dependent solution approaches that of the rate-independent theory (Perzyna, 1966). This can be appreciated noting that the numerator in the angle brackets in equation (5) is always smaller than the denominator, except on the yield surface, where the two are equal. Thus, when $m \to 0$, $\dot{\lambda}$ is equal to $\dot{\lambda}_0$ on the yield surface and vanishes in the interior. Furthermore, this approach allows one to maintain a step-by-step explicit implementation of the solution at all times.

We implemented this methodology in *Hercules*, an octree-based finite-element parallel computer-code for earthquake simulations developed by the Quake Group at Carnegie Mellon University (Tu *et al.*, 2006; Taborda *et al.*, 2010). Details of the implementation are provided in Taborda (2010).

CASE STUDIES

Case 1: The Mygdonian Basin

The first case considered is the Mygdonian basin, an east–west oriented graben divided by a ridge between the Volvi and the Lagada lakes in northern Greece (Fig. 1). This is one of the most seismoactive regions in Europe. The epicenter of the M_w 6.5 earthquake of 20 June 1978 was only a few kilometers north from the center of the valley, where European agencies established the Euroseistest project in 1993. The Euroseistest is a multipurpose test site and one of the longest running field laboratories of its type in the world (Pitilakis, 2008).

The valley is filled with sediments of two main geologic units, the Pro-Mygdonian and the Mygdonian systems. To the east, the deepest portion of the basin is located beneath Volvi Lake, reaching down to the bedrock at about 160 m. To the

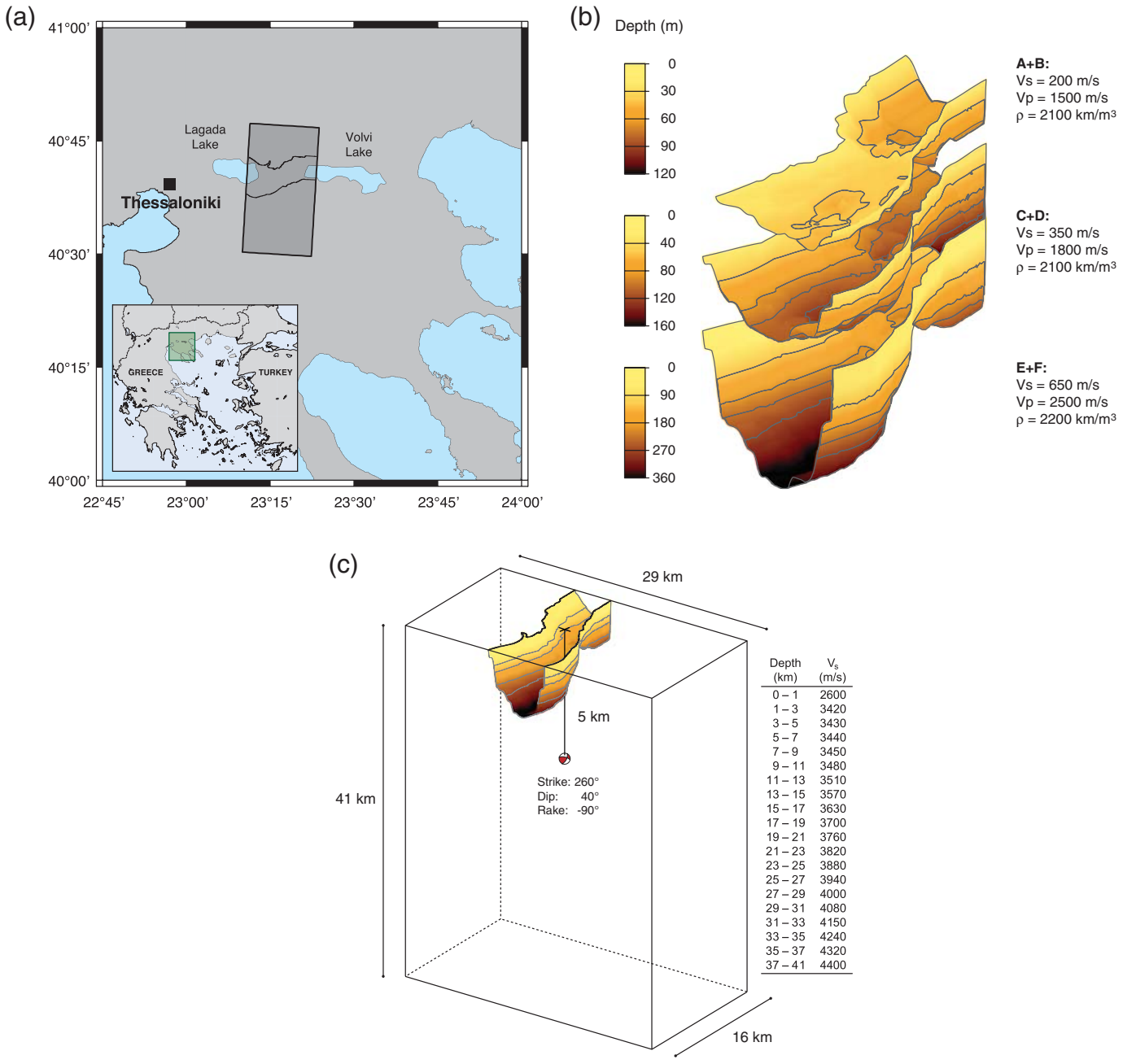

▲ **Figure 1.** The Mygdonian basin and the region of interest. (a) Location and surface projection of the simulation domain; (b) stratum depths and properties for the bottom of the three soil deposits; and (c) simulation domain and bedrock layer properties.

west, beneath Lagada Lake, the basement is found at about 370 m in depth. The different soil deposits in the basin have been categorized in six groups (A–F). Detailed information on the seismic conditions, geological structure, and geomechanical characteristics of the region can be found in the literature (e.g., Pitilakis *et al.*, 1999; Raptakis *et al.*, 2000).

We model the basin following the benchmark defined by the Euroseistest Verification and Validation Project (Bard *et al.*, 2008). The simulation domain consists of a volume of size 29 km × 16 km × 41 km. The properties of soil deposits within the basin are condensed into three strata ($A + B$, $C + D$, and $E + F$) with shear-wave velocities $V_S = 200$, 350, and 650 m/s, resting on a bedrock with values of V_S varying from 2600 m/s near the surface to 4400 m/s at the bottom of the domain (Fig. 1). Only the deposits within the basin (with $V_S \leq 650$ m/s) were allowed to deform plastically. Nonlinear-soil parameters are discussed later.

In this case we consider a hypothetical earthquake scenario of magnitude M_w 5.2, characterized by a point source located 5 km beneath the center of the basin. The source had a slip rate with corner frequency about 3 Hz, with a smooth decay between 3 and 4 Hz. The effective minimum shear-wave velocity and maximum frequency of the simulation were 200 m/s and 4 Hz, respectively. The elements in the FE model were tailored to conform to the geometry and material properties of the region following the rule $e = V_S^e/(f_{\max} p)$, in which e is the size of the element, V_S^e is an average value of the shear velocity within the element, $f_{\max}$ is the maximum frequency of the simulation, and p is the number of points per wavelength. In our applications, p is taken as 8, but due to the octree-based structure used in *Hercules*, the actual p varies between 8 and 14 (see Tu *et al.*, 2006; Bielak *et al.*, 2010). This results in a mesh with element sizes varying between 5 and 80 m.

We recognize that a moderate earthquake such as this would not be typically regarded as an event that is strong enough to generate plastic deformations in soil deposits. However, using a stronger event in the lack of a plausible extended source description would have resulted in largely unrealistic levels of ground-motion response. Therefore, we chose to limit our analysis to the idealized conditions and low-yield levels described, with the objective of evaluating the implementation of the methodology presented previously and assessing the response only qualitatively.

Case 2: The Salt Lake City Basin

In the second case we consider the Wasatch fault region in the north-central United States. We focus on the Salt Lake basin and the main urban areas in Salt Lake City, Utah (Fig. 2). Numerous studies have been devoted to understanding the seismicity and faulting characteristics of the Wasatch Front (e.g., Arabasz *et al.*, 1980; Machette *et al.*, 1991). Although these studies have shown that there is geologic evidence for the Wasatch fault to generate a moderate- to large-magnitude earthquake greater than 6.8, limited work has been devoted to estimating the levels of ground motion to be expected during such an event in the Salt Lake area. This has been mainly due to the lack of strong-motion records for large events in the region.

Recent efforts, however, have contributed additional tools and information about the geological and geotechnical characteristics, faulting mechanisms, and expected levels of ground shaking in the region (Magistrale *et al.*, 2006; Archuleta, 2011; Roten *et al.*, 2011; Wong *et al.*, 2011). We build upon these efforts to evaluate our implementation in conditions of higher material heterogeneity and for a more realistic earthquake source.

We model the basin in a volume domain of size 60 km × 45 km × 30 km as in Roten *et al.* (2011), using the Wasatch Front Community Velocity Model (version 3c) developed by Magistrale *et al.* (2006). We consider an earthquake scenario of magnitude M_w 6.8. The source model corresponds to a rupture of the Salt Lake City segment of the Wasatch fault (Archuleta, 2011). It consists of a set of 46 × 101 asperities in a fault plane of an area of 28.7 × 16.6 km^2, oriented with a strike and dip of 153° and 50°, respectively. All asperities are normal subfaults with a rake of 0° (see Fig. 2b).

As in the first case, the FE mesh was refined to conform to the geometry and material properties of the region. Here, however, we used a minimum shear-wave velocity, $V_{S_{\min}} = 200$ m/s and a maximum frequency, $f_{\max} = 1$ Hz. This resulted in an element size variation between about 15 and 450 m at the shallower soft-soil deposits and rock, respectively. Although we recognize that nonlinear soil behavior has been predominantly observed at frequencies larger than 0.5 Hz, we faced numerical difficulties throughout the simulation process that required us to limit the simulation parameters to $f_{\max} = 1$ Hz. These issues are addressed in the following sections and in the Final Remarks and Conclusions. In this case, only the soil deposits with $V_S \leq 500$ m/s were allowed to deform plastically.

NONLINEAR SOIL PARAMETERS

The implementation available in *Hercules* uses a Drucker–Prager (elasto-plastic) yield criterion. We have, however, not yet implemented other aspects relevant to the behavior of the nonlinear model such as hardening in the material or the contribution of the effective (vertical) stress in the soil due to geostatic consolidation of the volume above each element. Therefore, as a first approximation, we only consider nonlinearity in the shear deformation; thus, the material was idealized to conform to the von Mises yield criterion:

$$f(\sigma_{ij}) = \sqrt{J_2} - k = 0, \tag{7}$$

where J_2 is the second invariant of the stress deviator tensor, and k is a constant that depends on the material's elastic limit, usually expressed in terms of the octahedral shear stress, τ_{oct}.

For site-specific studies, plastic parameters are determined through experimental tests. This information, however, is not available for regional continuous models such as those considered here. Therefore, we assigned the elastic limits based on the

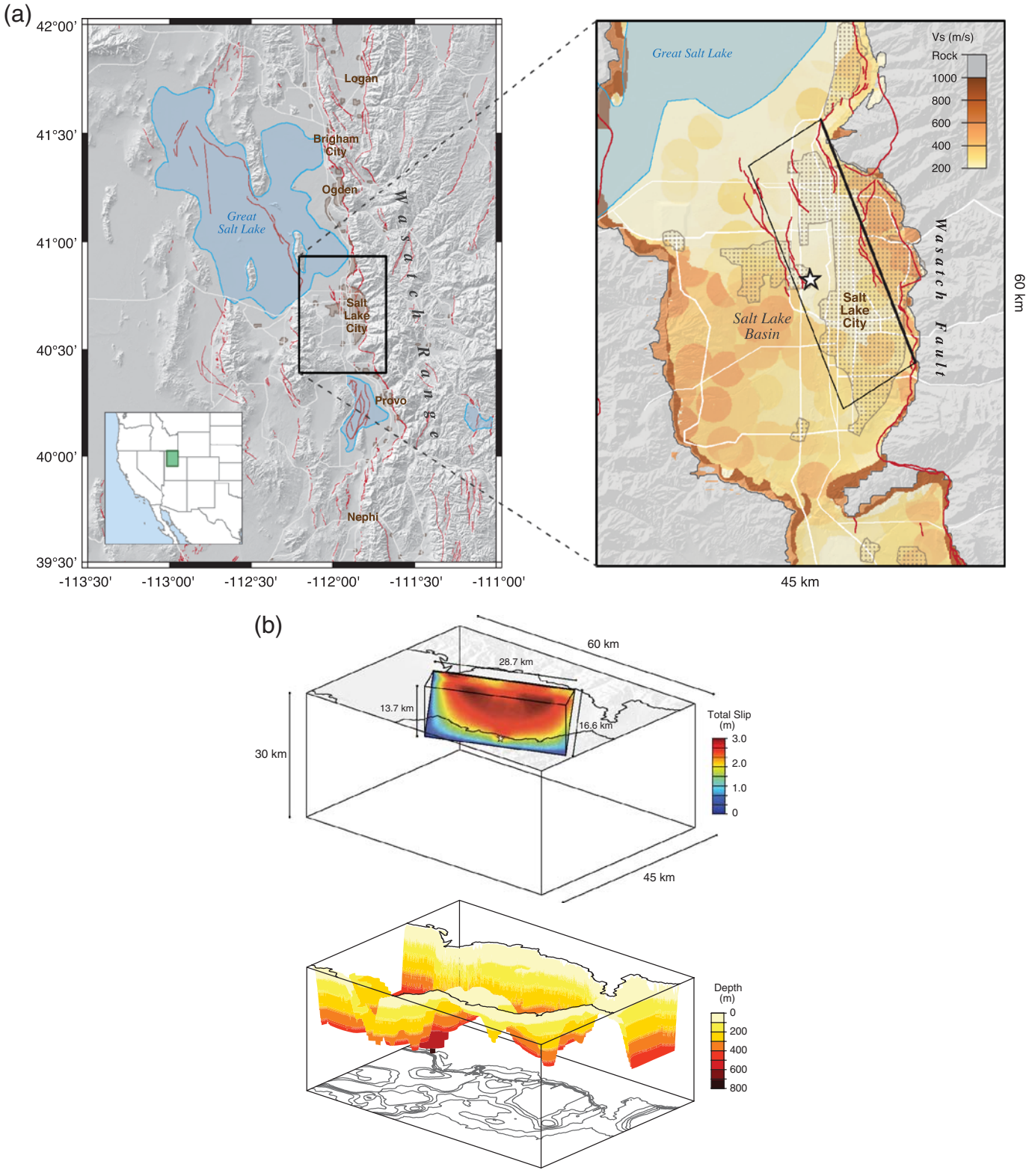

▲ **Figure 2.** (a) Left: The Wasatch Front and quaternary faults in the region. Right: Horizontal projection of the simulation domain, values of surface shear-wave velocities, and projection of the fault plane. Dotted areas indicate urban limits and the star shows the location of the epicenter. (b) Top: Simulation domain and total slip on the fault. Bottom: Basin depth at $V_S = 1000$ m/s.

stress levels observed during the initial linear-anelastic reference run. In each case, we first ran a simulation under linear conditions and stored the history of J_2 at all elements with material properties below a predefined V_S threshold (650 and 500 m/s for cases 1 and 2, respectively). Then, we artificially set an elastic limit value for k as a fraction of the maximum values recorded for J_2.

In case 1, the values of k assigned for $V_S = 200$, 350, and 650 m/s corresponded to 15%, 30%, and 50% of the peak value of $\sqrt{J_2}$ obtained during the reference run, respectively. In case 2, however, there were no distinct strata, which made setting these artificial elastic limits more difficult. Although in principle, the simulation itself should dictate whether the soil will or will not respond in the nonlinear regime, as mentioned previously, we had not yet implemented the necessary operations to make this happen. Instead, we built a statistical account of the history of $\sqrt{J_2}$ for all elements within a threshold of $V_S \leq 500$ m/s and assigned the yielding limits based on the peak values of $\sqrt{J_2}$ obtained during the anelastic simulation. The threshold of $V_S \leq 500$ m/s was set as a means to constrain plastic behavior to the upper layers, because it is expected that deeper deposits have higher levels of strength due to overburden pressures. In addition, the isosurface at $V_S = 500$ m/s provided a good approximation of the geometry of the basin deposits. We then set a yielding limit of about 20% the maximum values of $\sqrt{J_2}$. On average, the yielding limit k was set to about 20% the maximum values of the linear results for $\sqrt{J_2}$. In both cases, these limits were set arbitrarily to procure a noticeable nonlinear effect on the ground motion for the particular scenario earthquake considered.

Case 2 required some additional simplifications to guarantee the numerical stability of the simulation. Given that the source rupture is represented by an equivalent (kinematic) set of forces applied at the nodes of the FE mesh, elements intersected by the fault and in its immediate vicinity experience very large (unrealistic) deformations. This artificial effect vanishes with distance. Near the fault, however, it poses numerical problems. To avoid these artifacts and others due to the free-surface conditions, we set the elements in the neighborhood of the fault plane (≤ 500 m) and those at the surface to remain linear. We estimated the impact of these simplifications on the overall response of the valley for a set of simulations with alternate cases where such accommodations were unnecessary (e.g., with a fault plane that does not break to the surface nor does it cut through soft-soil elements); we found the impact of such simplifications to be negligible (less than 1% of the peak ground response).

We recognize that the results drawn from arbitrarily fixing the yielding limit of soft-soil deposits and the further simplifications necessary for case 2 are not sufficiently accurate for an analysis of the expected ground-motion response in these regions, but only a qualitative one that allows us to test the

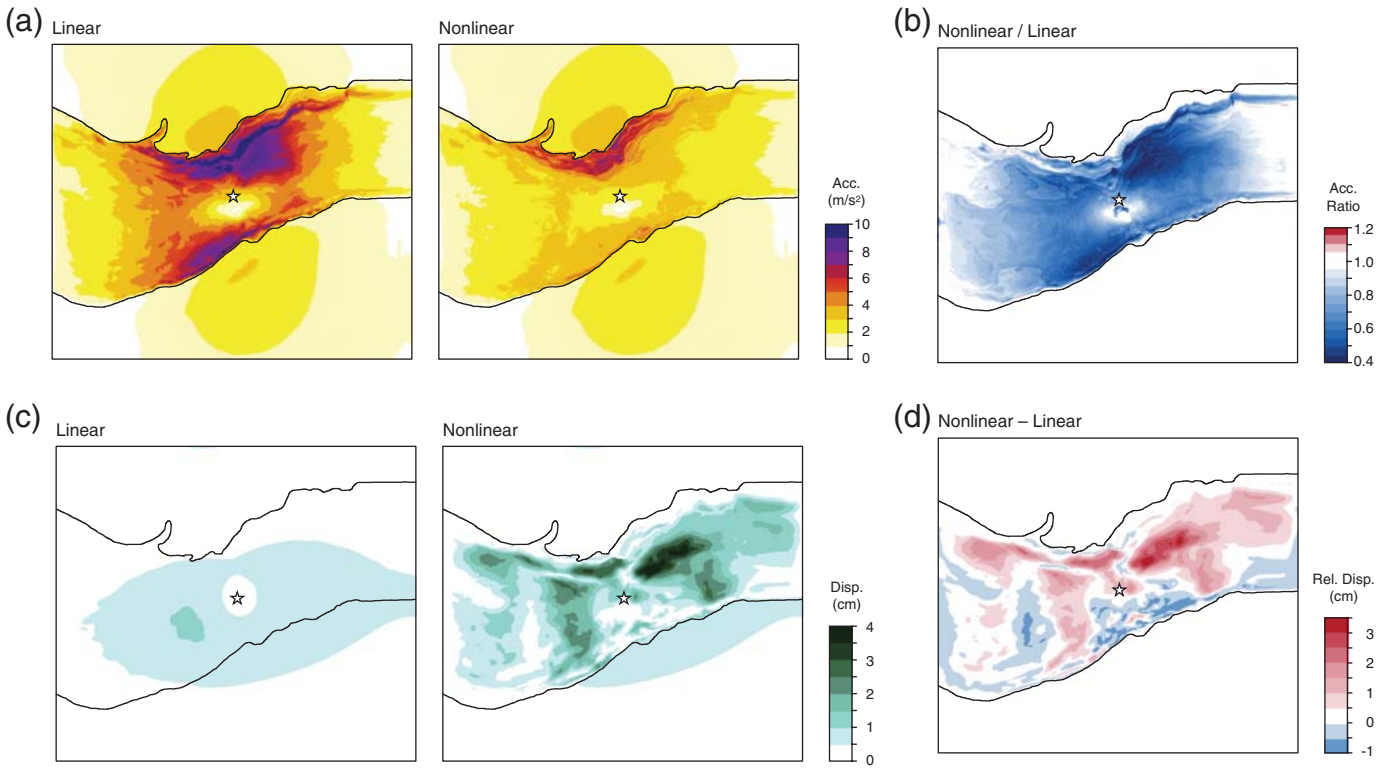

▲ **Figure 3.** Surface response of the Mygdonian basin under linear and nonlinear conditions. (a) Peak magnitudes of the surface horizontal acceleration; (b) ratio between the nonlinear and linear accelerations; (c) magnitude of the surface horizontal permanent displacement; and (d) difference between the linear and nonlinear permanent displacements. For reference, the contour line indicates the edge of the basin and the location of the epicenter is shown with a star.

implementation and give us a first approximation of the effects of nonlinearity in the soil on the ground motion in the context of regional large-scale simulations.

RESULTS

Case 1: The Mygdonian Basin

Figure 3 shows the response of the basin at the free surface under linear and nonlinear conditions in terms of the magnitude of the peak horizontal acceleration and of the permanent horizontal displacements, and their ratio and difference, respectively. Magnitudes are computed as the square root of the sum of the squares of the two horizontal components of motion, east–west and north–south.

The magnitude of accelerations shows no difference between the linear and nonlinear results outside the basin. This was expected given the high (soil-to-rock) contrast at the basin's boundary. Inside the basin, however, the accelerations under nonlinear conditions are pervasively smaller than in the linear simulation, with the minimum and maximum ratios equal to 0.32 and 1.42. Ratios greater than one, however, are barely noticeable. In a histogram analysis done for ratios less than 1.0, leaving out those values corresponding to points out of the basin or very close to 1.0, but just below the limit, we found the distribution to be centered at the upper values with median at about 0.72. Prevalent values correspond to reduction factors in the soil-to-rock ratios between 1.1 and 3. Given the idealized conditions imposed on the simulation parameters and the simplified plastic model used, these results are not directly comparable to average reduction factors of about 2 observed in previous studies (e.g., Beresnev *et al.*, 1995; Field *et al.*, 1997). They are, however, a promising example of the potential of reproducing realistic nonlinear effects in the future, once we address other missing aspects in our models.

Figure 3 also shows that in terms of permanent displacements, nonlinearity in the soil drastically changes the spatial distribution of permanent displacements within the basin. From the difference between the two simulations it is seen that the magnitude of permanent displacements tends to be larger in the nonlinear case, especially toward the north edge

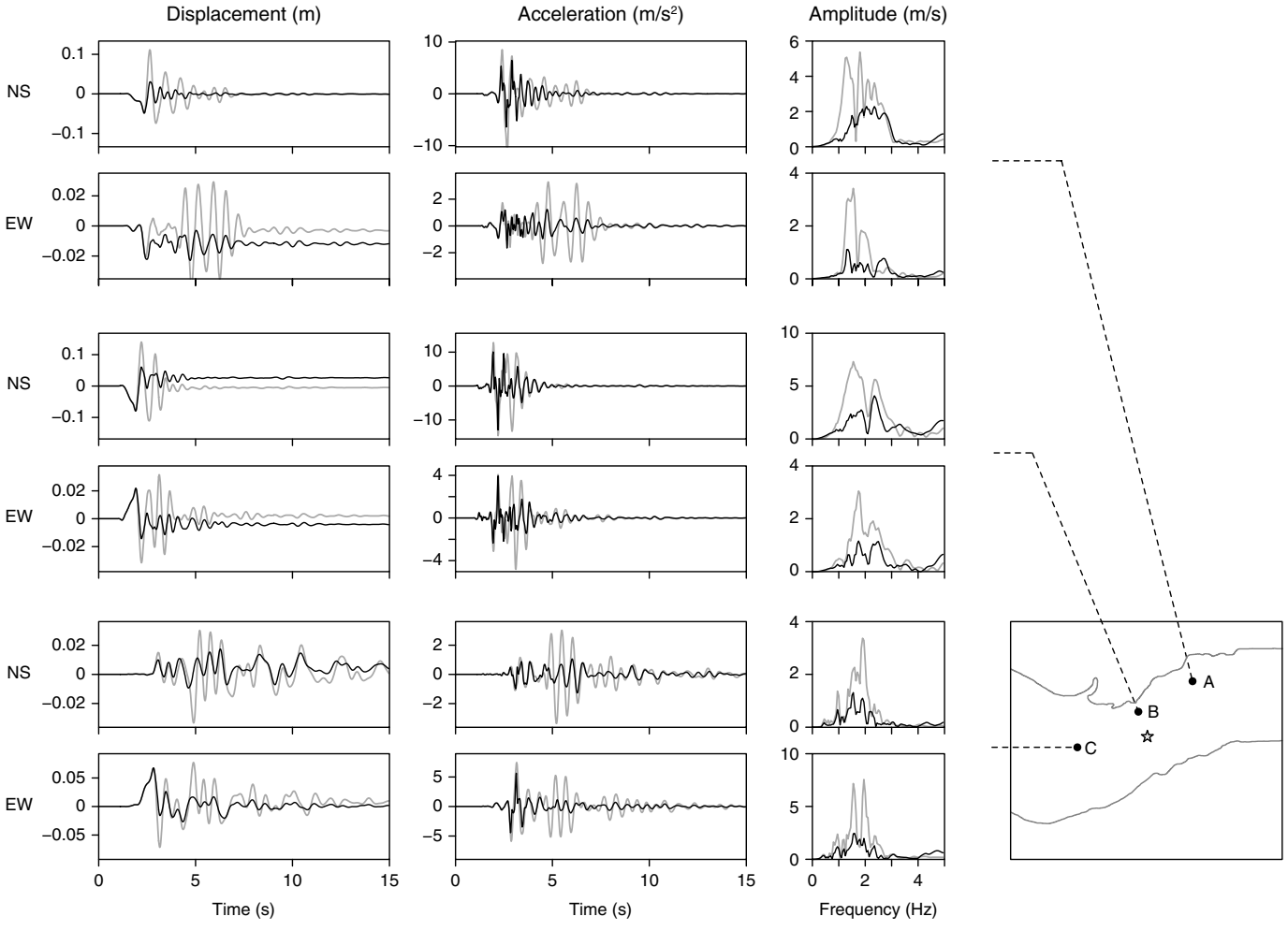

▲ **Figure 4.** Surface east–west and north–south displacement and acceleration histories, and Fourier amplitude spectra of accelerations at three stations A, B, and C (indicated with dots) located west, north, and northeast from the epicenter (indicated with a star). Gray lines correspond to the linear simulation, and black lines correspond to the nonlinear case.

and northeast area of the basin. Both the magnitude of accelerations and permanent displacements make evident the continued presence of basin and edge effects in the nonlinear case.

Figure 4 shows the histories of displacement and acceleration, and the Fourier amplitude transform of acceleration for three observation points (or stations) A, B, and C, located to the northeast, north, and west of the epicenter, respectively. Station A, for instance, shows significant changes in displacement amplitudes in the north–south and east–west components, and in the east–west permanent displacement. Station B also exhibits changes in the displacement in both components. Station C shows no significant change in the permanent displacement, but it does present a significant reduction in the amplitudes of accelerations, greater than the reductions observed in A and B. We believe stations A and B, being located near the edge and above shallower basin deposits, exhibit a stronger effect in the displacements than station C, because their response was more closely associated with local plastic deformations, as opposed to station C, where the changes observed are the result of nonlinear effects carried over from the deeper layers. In the frequency domain, the bulk of energy loss due to plastic deformations across stations is concentrated between 1 and 3 Hz. This is, despite the simplifications made in our model, consistent with though not necessarily equivalent to previous observations (e.g., Darragh and Shakal, 1991; Field *et al.*, 1997; Beresnev, 2002).

At the element level, nonlinearity can be observed in terms of the stress-strain relationships as intrinsic functions of time. Figure 5 shows these results for an array of points in depth, at a station east from the epicenter. The largest plastic-deformations are observed at 25, 75, and 100 m in depth in the 200 and 350 m/s strata. Values of deformation where plasticity occurred are of the order of 4×10^{-4} and greater, consistent with previous observations. Notice that the coupling between the three components *xy*, *yz*, and *xz* of the stress-strain relationships makes evident the existence of significant 3D effects, which could not be reproduced using 1D approaches. We found that most plastic excursions occur early in the simulation, between 2 and 4 s.

Case 2: The Salt Lake City Basin

Figure 6 shows the magnitude of accelerations and permanent displacements, along with the ratio and difference comparisons between linear and nonlinear response for the Salt Lake City basin simulations. In terms of acceleration, we observe a considerable reduction in the levels of peak response. In this case, however, basin effects are less significant; the most prominent changes are concentrated near the fault and toward the north, at the deepest part of the basin. There are almost no differences between the linear and nonlinear results toward the south.

The ratio of peak acceleration magnitudes is also different from the previous case because in this simulation we observe amplifications in the nonlinear results, as seen from the ratios > 1 near the center of the basin, and southwest and northwest from the epicenter. They are still relatively small and not as widespread as the ratios < 1. Ratios reach isolated values as low as 0.12, but are predominant above 0.25. This corresponds to reduction factors of peak magnitude acceleration up to 4, with an average reduction factor of about 1.75. In contrast with

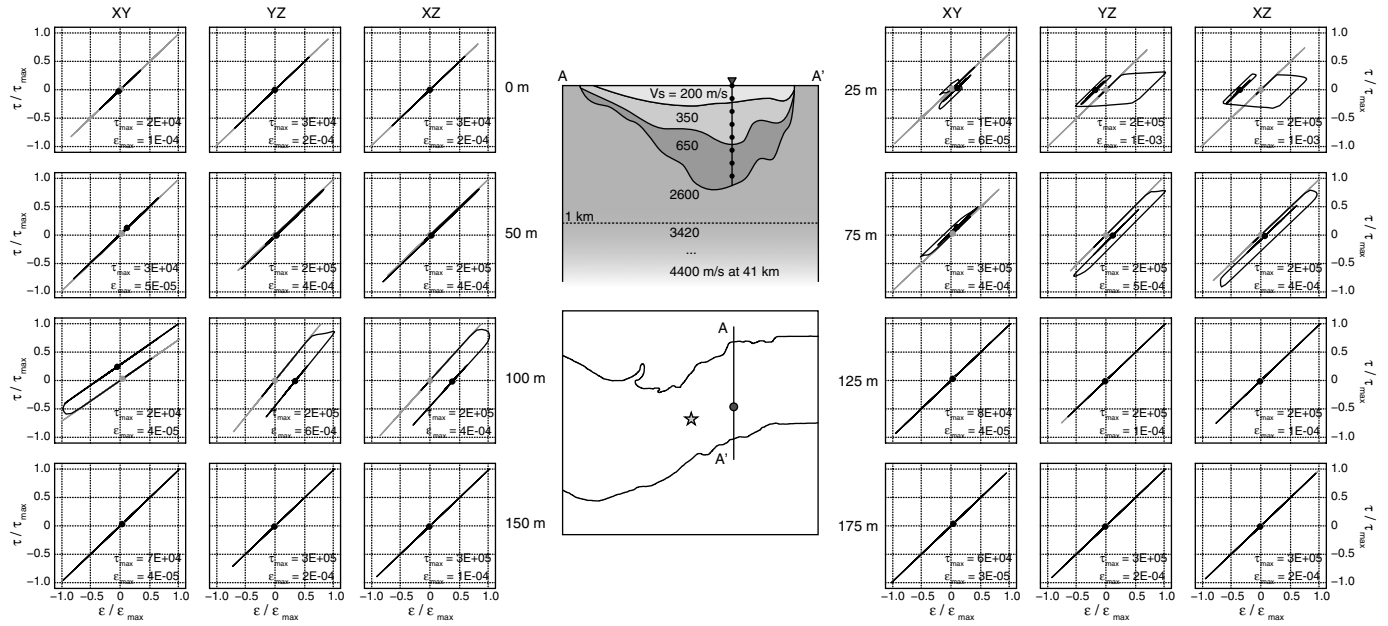

▲ **Figure 5.** Stress-strain relationships as implicit functions of time along an array of points beneath a station (dot) located east from the epicenter (star). Gray lines correspond to the linear simulation, and black lines correspond to the nonlinear one. Dots indicate the final stress-strain state. Each history is normalized both in stresses and strains, and the normalizing values are shown inside each frame. The map shows the location of the free-surface station and a vertical cut of the soil profile.

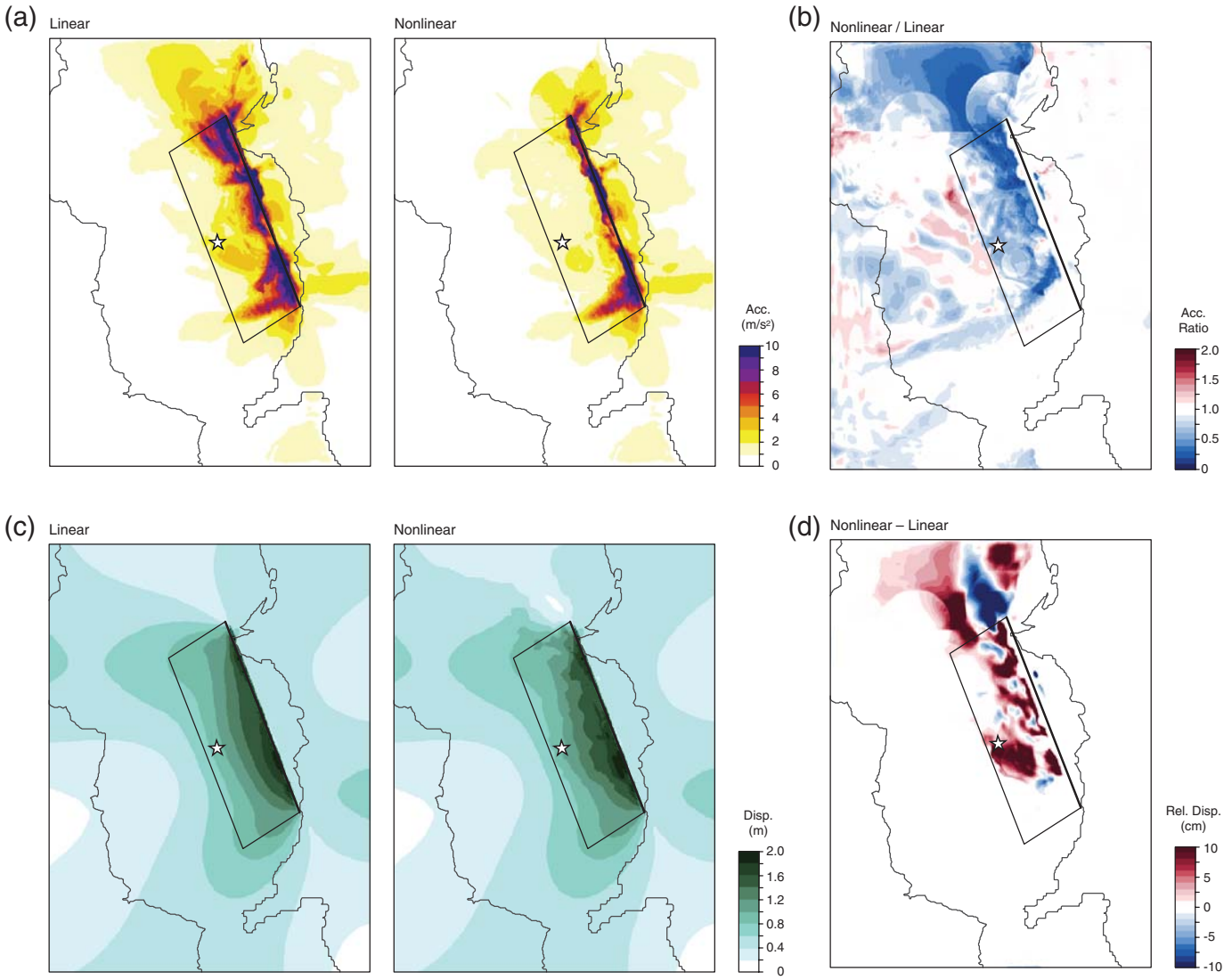

▲ **Figure 6.** Surface response of the Salt Lake City basin under linear and nonlinear conditions. (a) Peak magnitudes of the surface horizontal acceleration; (b) ratio between the nonlinear and linear accelerations; (c) magnitude of the surface horizontal permanent displacement; and (d) difference between the linear and nonlinear permanent displacements. For reference, the contour line indicates the edge of the basin and the rectangular shape shows the surface horizontal projection of the fault plane; the star within represents the location of the epicenter.

case 1, some differences are observed outside the basin. This is likely due to some level of refraction at the basin boundaries.

In terms of permanent displacements, notice that the source, with an average slip equal to 1.69 m (see Fig. 2 for reference), imposes significant levels of deformation near the fault line. Therefore, both the linear and nonlinear cases show strong correlation with the slip distribution and source radiation pattern, but in the nonlinear case, the presence of nonlinearity adds some level of spatial variability not present in the linear case. These added perturbations are seen from the differences concentrated along the fault and to the north. Their magnitude is about 5% to 10% of the magnitude of the maximum permanent displacements. For the most part, the nonlinear simulation presents larger permanent displacements than the linear one, with the exception of the area beyond the north end of the fault. Observing smaller permanent deformations in the nonlinear case challenges, in some sense, the idea that permanent deformations are always larger in the presence of nonlinearity. It is likely that in this particular case, this was influenced by 3D and basin effects, and by the proximity to the fault-plane breaking to the surface and experiencing significant slip.

Figure 7 shows the displacement, the acceleration histories, and the Fourier amplitude transforms of acceleration for a collection of stations distributed throughout the region. Nonlinear effects on the displacements are particularly noticeable in stations S5 through S9, and most prominent in stations S6 and S8. As we saw from Figure 6, nonlinearity, however, does not always result in larger permanent displacements. In particular, permanent deformations were larger in the nonlinear

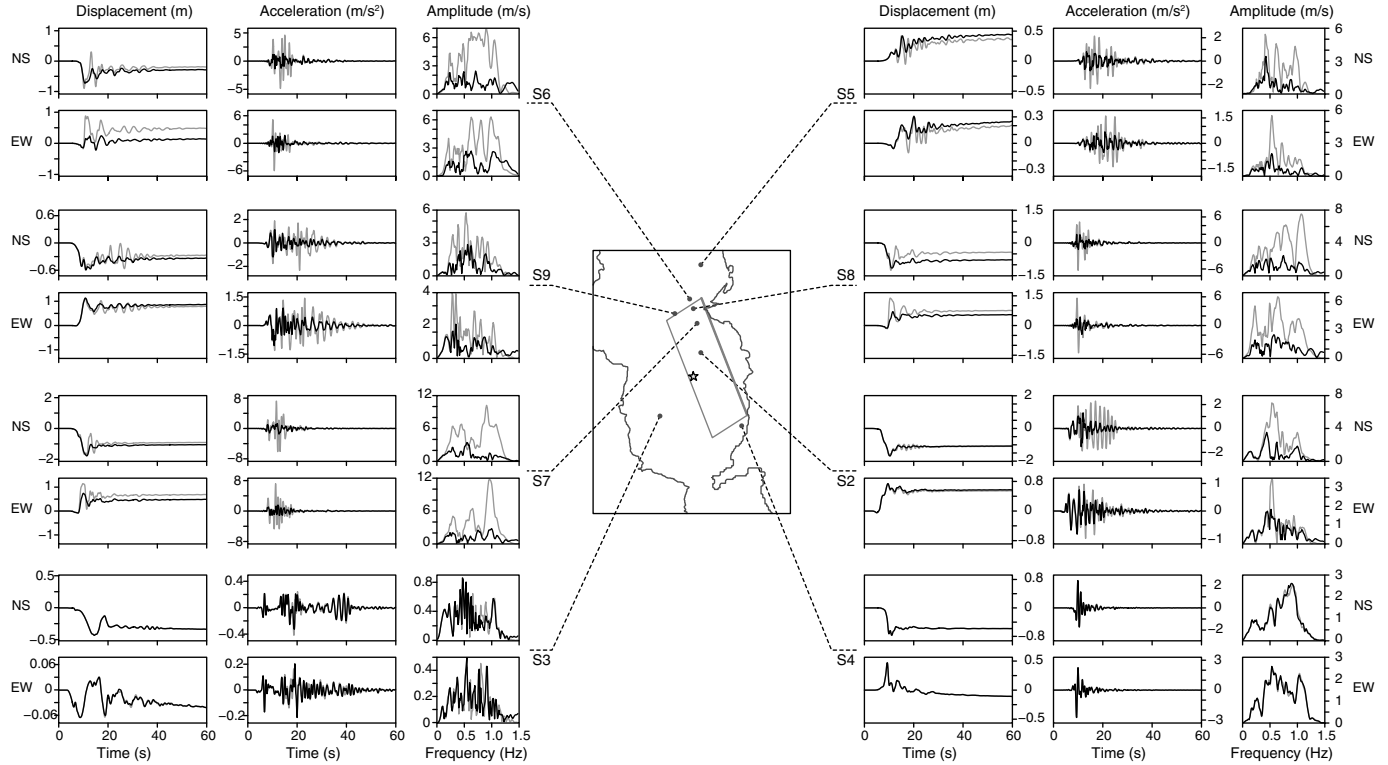

▲ **Figure 7.** Surface east–west and north–south displacement, acceleration histories, and Fourier amplitude spectra of accelerations at eight stations throughout the region of interest. Gray lines correspond to the results from the linear simulation, and black lines correspond to the nonlinear case. In the map, the dots and a star indicate the location of the stations and the epicenter, respectively; and the contour line and rectangular shape correspond to the edge of the basin and the surface horizontal projection of the fault plane.

simulation at stations S6, S7, and S8 in the north–south (fault parallel) component, and in stations S5 and S9 in the two components, whereas the linear permanent displacement was larger in the east–west (fault normal) components of stations S6, S7, and S8. Changes in acceleration, on the other hand, are observed in all stations, except S3 and S4, which are in areas where no relevant nonlinear effects were observed. In general, the amplitude of accelerations is reduced considerably within 5 and 30 s of simulation. Reductions in frequency are distributed between 0.25 and 1.0 Hz, with some predominance toward the higher frequencies. While nonlinear effects in displacements are typically correlated with local plastic deformations, the effects observed in the accelerations seem to be the result of a cumulative effect from the regional ground motion, as implied from the response of station S2 in the north–south component.

Finally, Figure 8 shows the stress-strain relationships for an array of points beneath a station north of the epicenter. Here, the largest deformations occur at 175 and 200 m, where strains in the nonlinear case reach values larger than twice the maximum linear strain. Although in this case the larger deformations occur at the bottom of the strata, near the limiting value of $V_S \leq 500$ m/s, the figure shows that a significant level of coupling exists between the three components (xy, yz, and xz) of the shear stress and strain tensors. This suggests the presence of significant 3D effects that could not be captured by 1D or 2D nonlinear analyses. As in the previous case, plastic excursions happened early in the simulation, remaining in the elastic regime afterward.

FINAL REMARKS AND CONCLUSIONS

We presented a methodology for modeling 3D nonlinear soil behavior in large-scale earthquake ground-motion simulations, and tested its implementation in a finite-element parallel simulation code for two case studies in realistic basins under idealized conditions. As a first approximation, we used a perfectly elasto-plastic model that considers plasticity only in the shear deformation, and set the soil parameters arbitrarily to force the occurrence of significant nonlinear behavior in the upper soft-soil deposits in the basins. Comparisons of nonlinear results with respect to the response under linear anelastic conditions indicate that soil nonlinearities may cause significant changes in the distribution of permanent displacements, and reductions in peak ground accelerations down to amplitudes as low as 20% of the peak response obtained under linear conditions. Although these results are, in some sense, qualitatively comparable to observations from past earthquakes and aftershocks, they are not necessarily conclusive about the expected level of nonlinear effects because of the simplifications and assignment of inelastic soil properties made at the constitutive level. Furthermore, our implementation still does not cover other

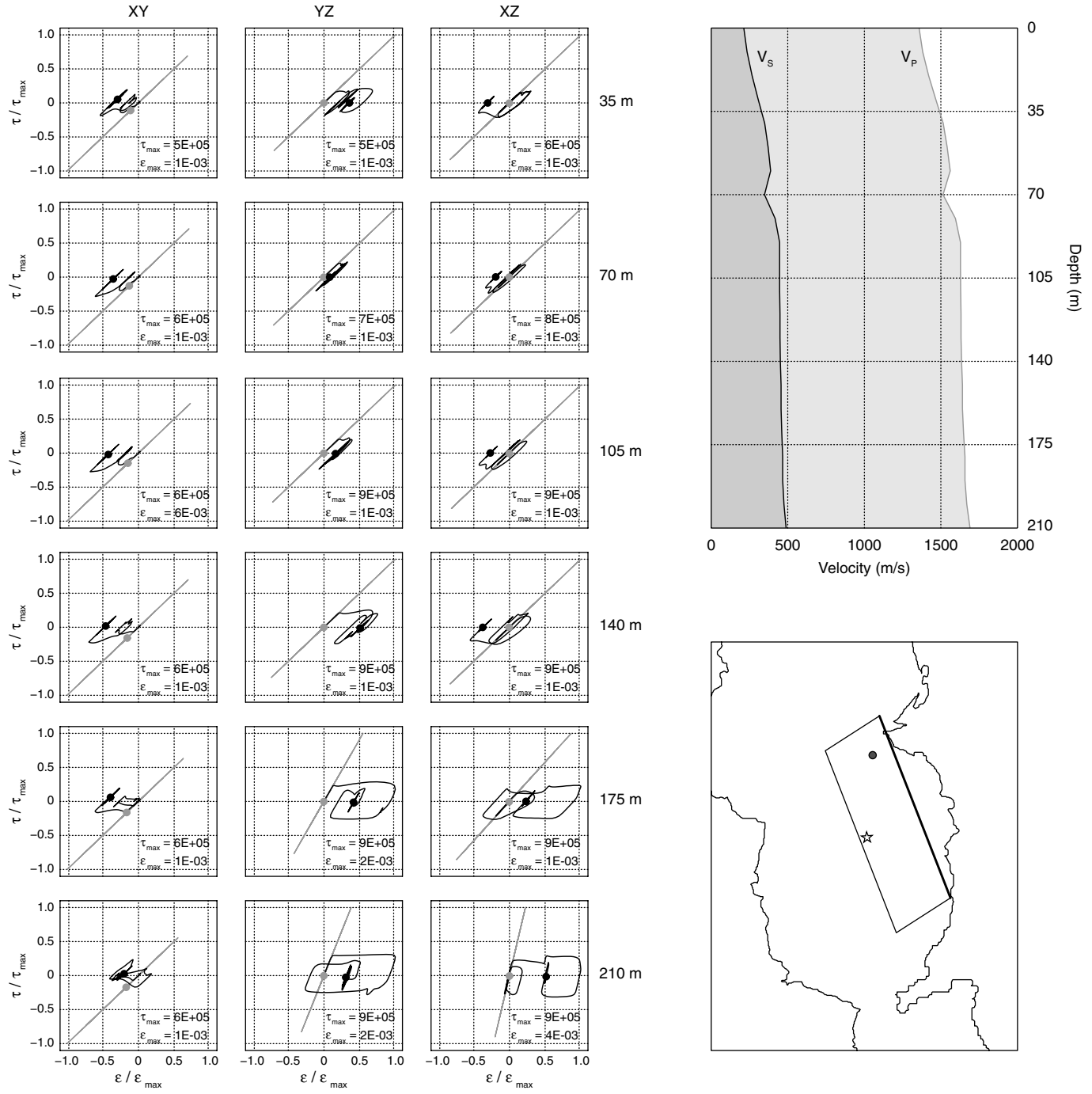

▲ **Figure 8.** Stress-strain relationships in depth as implicit functions of time along an array of points beneath a station located north of the epicenter (shown in the locational map with a dot and a star, respectively). Gray lines correspond to the linear simulation, and black lines correspond to the nonlinear one. Values are normalized with respect to the maximum values shown inside each frame, and the dots indicate the final stress-strain state. The profile of the seismic velocities along the array is shown on the right, along with the map indicating the location of the station.

aspects that are important to the nonlinear behavior of soil deposits such as the effective pressure due to geostatic consolidation or the effect of water-pore pressure. Our objective, nonetheless, was to test our implementation and evaluate its potential for regional large-scale 3D earthquake simulations.

Although we obtained acceptable results within the the conditions set in the simulations, we found that the methodology presented here posed significant modeling and numerical challenges. Although much simpler in principle, because of the possibility of implementing a step-by-step explicit solution for

the displacement field, the rate-dependent approach used here turned out to be considerably sensitive to the heterogeneity and transient nature of the seismic problem. As a result, the solution often diverged from the yield-function and the simulations had to be reset and run again using smaller time-steps. In the end, the nonlinear simulations used discrete-time sizes of the order of four to eight times smaller than those used in the linear simulations. In case 1, for instance, the linear simulation converged at a maximum time-step, $\Delta t = 0.002$ s, whereas the nonlinear simulation required a $\Delta t = 0.0005$. In case 2, the simulation time-steps changed from 0.005 s in the linear case to 0.00065 s in the nonlinear one. For a total simulation time of 20 and 75 s, the total simulation steps went from 10,000 to 40,000, and from 15,000 to 115,385. This resulted in larger consumption of computational time and resources.

We are currently working on the implementation of an alternative approach that uses a rate-independent methodology. Our initial tests suggest that this alternative is less sensitive to the issues faced with the rate-dependent approach, although it depends more delicately on the complexity of the constitutive model. We are also implementing a progressive loading approach that will allow us to consider the effective stress due to gravitational forces and consolidation. We expect to be able to improve the computational performance while maintaining a stable control on the numerical issues. We intend to present results of this alternative approach and a more realistic assignment of material properties in a future publication.

The initial results presented here, nonetheless, indicate that there are significant levels of 3D, source, and basin effects that may influence the presence and behavior of nonlinear soil effects in large-scale simulations beyond those that can be reproduced using 1D and 2D approaches. These results are relevant to the advancement, promotion, and use of physics-based earthquake simulations for characterizing site-response at local and regional scales.

ACKNOWLEDGMENTS

This work was supported by the National Science Foundation, the U.S. Geological Survey, and the Southern California Earthquake Center through awards: Towards Petascale Simulation of Urban Earthquake Impacts (NSF OCI-0749227); A Petascale Cyberfacility for Physics-Based Seismic Hazard Analysis (SCEC PetaSHA3 Project) (NSF EAR-0949443); Outward on the Spiral: Petascale Inference in Earthquake System Science (SCEC PetaShake Project) (NSF OCI-0905019); Hybrid Three-Dimensional Modeling of Earthquake Ground Motion in Basins, including Nonlinear Wave Propagation in soils (USGS 08HQGR0018); Three-Dimensional Nonlinear Earthquake Ground Motion Simulation in the Salt Lake Basin Using the Wasatch Front Community Velocity Model (USGS G10AP00077); and Implementation and Application of Inelastic Soil Models in Full 3D Earthquake Simulations (USGS G11AP20127). SCEC is funded by NSF Cooperative Agreement EAR-0529922 and USGS Cooperative Agreement 07HQAG0008. The SCEC contribution number for this paper is 1638. The third author was partially supported by a Fulbright-Colciencias-DNP award. This research was supported by an allocation of advanced computing resources supported by the National Science Foundation through the TeraGrid and XSEDE programs. The computations were performed on Kraken at the U.S. National Institute for Computational Sciences. We thank Emmanuel Chaljub from the Institut des Sciences de la Terre, Observatoire des Sciences de l'Univers at Université Joseph Fourier, Grenoble, France, for providing the model of the Mygdonian basin. We also thank the anonymous reviewer for comments and suggestions that helped us improve the paper.

REFERENCES

Aagaard, B. T., T. M. Brocher, D. Dolenc, D. Dreger, R. W. Graves, S. Harmsen, S. Hartzell, S. Larsen, and M. L. Zoback (2008). Ground-motion modeling of the 1906 San Francisco earthquake, Part I: Validation using the 1989 Loma Prieta earthquake, *Bull. Seismol. Soc. Am.* **98,** no. 2, 989–1011.

Aki, K. (2003). A perspective on the history of strong motion seismology, *Phys. Earth Planet. In.* **137,** no. 1–4, 5–11.

Arabasz, W. J., R. B. Smith, and W. D. Richins (1980). Earthquake studies along the Wasatch Front, Utah: Network monitoring, seismicity, and seismic hazards, *Bull. Seismol. Soc. Am.* **70,** no. 5, 1479–1499.

Archuleta, R. (2011). Strong ground motions in Salt Lake City and other metropolitan areas from large earthquakes on the Wasatch fault, *Tech. Rept. G09AP00027, U.S. Geol. Surv.*

Archuleta, R. J., P. Liu, J. H. Steidl, L. F. Bonilla, D. Lavallée, and F. E. Heuzé (2003). Finite-fault site-specific acceleration time histories that include nonlinear soil response, *Phys. Earth Planet. In.* **137,** no. 1–4, 153–181.

Assimaki, D., W. Li, J. Steidl, and J. Schmedes (2008). Quantifying nonlinearity susceptibility via site-response modeling uncertainty at three sites in the Los Angeles basin, *Bull. Seismol. Soc. Am.* **98,** no. 5, 2364–2390.

Bao, H., J. Bielak, O. Ghattas, L. F. Kallivokas, D. R. O'Hallaron, J. R. Shewchuk, and J. Xu (1998). Large-scale simulation of elastic wave propagation in heterogeneous media on parallel computers, *Comput. Meth. Appl. Mech. Eng.* **152,** no. 1–2, 85–102.

Bard, P.-Y., E. Chaljub, F. Hollender, M. Manakou, and K. Pitilakis (2008). Euroseistest numerical benchmark: Phase I, *Techn. rept., Commissariat à l'énergie atomique et aux énergies alternatives (CEA)*, Euroseistest verification and validation E2VP Cashima Project, Cadarache, France, June 2008, 14 pp.

Beresnev, I. A. (2002). Nonlinearity at California generic soil sites from modeling recent strong-motion data, *Bull. Seismol. Soc. Am.* **92,** no. 2, 863–870.

Beresnev, I. A., and K.-L. Wen (1996). Nonlinear soil response—A reality? *Bull. Seismol. Soc. Am.* **86,** no. 6, 1964–1978.

Beresnev, I. A., K.-L. Wen, and Y. Tein Yeh (1995). Nonlinear soil amplification: Its corroboration in Taiwan, *Bull. Seismol. Soc. Am.* **85,** no. 2, 496–515.

Bielak, J., R. W. Graves, K. B. Olsen, R. Taborda, L. Ramírez-Guzmán, S. M. Day, G. P. Ely, D. Roten, T. H. Jordan, P. J. Maechling, J. Urbanic, Y. Cui, and G. Juve (2010). The ShakeOut earthquake scenario: Verification of three simulation sets, *Geophys. J. Int.* **180,** no. 1, 375–404.

Chang, C. Y., M. S. Power, Y. K. Tang, and C. M. Mok (1989). Evidence of nonlinear soil response during a moderate earthquake, in *Proc. of the 12th Int. Conf. on Soil Mechanics and Foundation Eng.*, vol. 3, Rio de Janero, Brazil, 13–18 August 1989, 1927–1930.

Chin, B.-H., and K. Aki (1991). Simultaneous study of the source, path, and site effects on strong ground motion during the 1989 Loma Prieta earthquake: A preliminary result on pervasive nonlinear site effects, *Bull. Seismol. Soc. Am.* **81,** no. 5, 1859–1884.

Dafalias, Y. F. (1986). Bounding surface plasticity. I: Mathematical foundation and hypoplasticity, *J. Eng. Mech.* **112,** no. 9, 966–987.

Dafalias, Y. F., and E. P. Popov (1975). A model of nonlinearly hardening materials for complex loading, *Acta Mech.* **21,** no. 3, 173–192.

Darragh, R. B., and A. F. Shakal (1991). The site response of two rock and soil station pairs to strong and weak ground motion, *Bull. Seismol. Soc. Am.* **81,** no. 5, 1885–1899.

Dupros, F., F. de Martin, E. Foerster, D. Komatitsch, and J. Roman (2010). High-performance finite-element simulations of seismic wave propagation in three-dimensional nonlinear inelastic geological media, *Parallel Comput.* **36,** no. 5–6, 308–325.

Elgamal, A., L. Yan, Z. Yang, and J. P. Conte (2008). Three-dimensional seismic response of the Humboldt Bay bridge-foundation-ground system, *J. Struct. Eng.* **134,** no. 7, 1165–1176.

Faccioli, E., F. Maggio, R. Paolucci, and A. Quarteroni (1997). 2D and 3D elastic wave propagation by a pseudo-spectral domain decomposition method, *J. Seismology* **1,** no. 3, 237–251.

Field, E. H., P. A. Johnson, I. A. Beresnev, and Y. Zeng (1997). Nonlinear ground-motion amplification by sediments during the 1994 Northridge earthquake, *Nature* **390,** no. 6660, 599–602.

Field, E. H., S. Kramer, A.-W. Elgamal, J. Bray, N. Matasovic, P. Johnson, C. Cramer, C. Roblee, D. J. Wald, L. F. Bonilla, P. P. Dimitriu, and J. Anderson (1998). Nonlinear site response: Where we're at (A report from a SCEC/PEER seminar and workshop), *Seismol. Res. Lett.* **69,** no. 3, 230–234.

Finn, W. D. L., G. R. Martin, and M. K. W. Lee (1978). Comparison of dynamic analyses for saturated sands, in *Proc. of the ASCE Geotechnical Eng. Div. Specialty Conf.*, Earthquake Engineering and Soil Dynamics, Pasadena, California, 19–21 June 1978, 472–491.

Frankel, A., and J. Vidale (1992). A three-dimensional simulation of seismic waves in the Santa Clara Valley, California, from a Loma Prieta aftershock, *Bull. Seismol. Soc. Am.* **82,** no. 5, 2045–2074.

Graves, R. W. (1998). Three-dimensional finite-difference modeling of the San Andreas fault: Source parameterization and ground-motion levels, *Bull. Seismol. Soc. Am.* **88,** no. 4, 881–897.

Hardin, B. O., and V. P. Drnevich (1972). Shear modulus and damping in soils: Measurement and parameters effects, *J. Soil Mech. Found. Div., ASCE* **98,** no. SM6, 603–624, paper 8977.

Hartzell, S., A. Leeds, A. Frankel, R. A. Williams, J. Odum, W. Stephenson, and W. Silva (2002). Simulation of broadband ground motion including nonlinear soil effects for a magnitude 6.5 earthquake on the Seattle fault, Seattle, Washington, *Bull. Seismol. Soc. Am.* **92,** no. 2, 831–853.

Idriss, I. M., and H. B. Seed (1968). An analysis of ground motions during the 1957 San Francisco earthquake, *Bull. Seismol. Soc. Am.* **58,** no. 6, 2013–2032.

Idriss, I. M., and J. I. Sun (1993). *User's manual for SHAKE91: A computer program for conducting equivalent linear seismic response analyses of horizontally layered soil deposits*, Center for Geotechnical Modeling, Dept. of Civil and Environmental Engineering, University of California, Davis, California.

Joyner, W. B., and A. T. F. Chen (1975). Calculation of nonlinear ground response in earthquakes, *Bull. Seismol. Soc. Am.* **65,** no. 5, 1315–1336.

Komatitsch, D., and J.-P. Vilotte (1998). The spectral element method: An efficient tool to simulate the seismic response of 2D and 3D geological structures, *Bull. Seismol. Soc. Am.* **88,** no. 2, 368–392.

Machette, M. N., S. F. Personius, A. R. Nelson, D. P. Schwartz, and W. R. Lund (1991). The Wasatch fault zone, Utah—Segmentation and history of Holocene earthquakes, *J. Struct. Geol.* **13,** no. 2, 137–149.

Magistrale, H., K. B. Olsen, and J. C. Pechmann (2006). Construction and verification of a Wasatch Front Community Velocity Model, *Tech. Rept. 06HQGR0012*, *U.S. Geol. Surv.*, 14 pp.

Olsen, K. B., R. J. Archuleta, and J. R. Matarese (1995). Three-dimensional simulation of a magnitude 7.75 earthquake on the San Andreas fault, *Science* **270,** no. 5242, 1628–1632.

Perzyna, P. (1963). The constitutive equations for rate sensitive plastic materials, *Q. Appl. Math.* **20,** 321–332.

Perzyna, P. (1966). Fundamental problems in viscoplasticity, in *Advances in Applied Mechanics*, G. Chernyi, H. Dryden, P. Germain, L. Howarth, W. Olszak, W. Prager, R. Probstein, and H. Ziegler (Editors), Vol. **9**, Elsevier, Amsterdam, 243–377.

Pitilakis, K. (2008). EUROSEISTEST: A European test site for engineering seismology, earthquake engineering and seismology, *Tech. rept.*, Department of Civil Engineering, Aristotle University of Thessaloniki, Thessaloniki, Greece.

Pitilakis, K., D. Raptakis, K. Lontzetidis, T. H. Tika-Vassilikou, and D. Jongmans (1999). Geotechnical and geophysical description of Euro-seistest, using field, laboratory tests and moderate strong motion records, *J. Earthquake Eng.* **3,** no. 3, 381–409.

Prévost, J.-H. (1977). Mathematical modelling of monotonic and cyclic undrained clay behaviour, *Int. J. Numer. Anal. Meth. Geomech.* **1,** no. 2, 195–216.

Prévost, J.-H. (1985). A simple plasticity theory for frictional cohesionless soils, *Soil Dynam. Earthquake Eng.* **4,** no. 1, 9–17.

Raptakis, D., F. J. Chávez-García, K. Makra, and K. Pitilakis (2000). Site effects at Euroseistest-I. Determination of the valley structure and confrontation of observations with 1D analysis, *Soil Dynam. Earthquake Eng.* **19,** no. 1, 1–2.

Roten, D., K. Olsen, J. C. Pechmann, V. M. Cruz-Atienza, and H. Magistrale (2011). 3D simulations of *M* 7 earthquakes on the Wasatch fault, Utah, Part I: Long-period (0–1 Hz) ground motion, *Bull. Seismol. Soc. Am.* **101,** no. 5, 2045–2063.

Schnabel, P. B., J. Lysmer, and H. B. Seed (1972). SHAKE: A computer program for earthquake response analysis of horizontally-layered sites, *Tech. Rept. EERC-72/12*, Earthquake Engineering Research Center, University of California, Berkeley, California.

Schnabel, P., H. B. Seed, and J. Lysmer (1972). Modification of seismograph records for effects of local soil conditions, *Bull. Seismol. Soc. Am.* **62,** no. 6, 1649–1664.

Seed, H. B., and I. M. Idriss (1969). Influence of soil condition on ground motions during earthquakes, *J. Soil Mech. Found. Div.* **95,** no. SM1, 99–137, paper 6347.

Seriani, G. (1998). 3-D large-scale wave propagation modeling by spectral element method on Cray T3E multiprocessor, *Comput. Meth. Appl. Mech. Eng.* **164,** no. 1–2, 235–247.

Streeter, V. L., E. B. Wylie, and F. E. Richart (1974). Soil motion computations by characteristics method, *J. Geotech. Eng. Div.* **100,** no. 3, 247–263.

Taborda, R. (2010). Three Dimensional Nonlinear Soil and Site-City Effects in Urban Regions, *Ph.D. Thesis*, Civil and Environmental Engineering, Carnegie Institute of Technology, Carnegie Mellon University, Pittsburgh, Pennsylvania.

Taborda, R., J. López, H. Karaoglu, J. Urbanic, and J. Bielak (2010). Speeding up finite element wave propagation for large-scale earthquake simulations, *Tech. Rept. CMU-PDL-10-109*, Carnegie Mellon University, Parallel Data Lab, Pittsburgh, Pennsylvania.

Trifunac, M. D., and M. I. Todorovska (1996). Nonlinear soil response—1994 Northridge, California, earthquake, *J. Geotech. Eng.* **122,** no. 9, 725–735.

Tu, T., H. Yu, L. Ramírez-Guzmán, J. Bielak, O. Ghattas, K.-L. Ma, and D. R. O'Hallaron (2006). From mesh generation to scientific visualization: An end-to-end approach to parallel supercomputing, in *SC06: Proc. of the 2006 ACM/IEEE Int. Conf. for*

High Performance Computing, Networking, Storage and Analysis, IEEE Computer Society, Tampa, Florida, 11–17 November 2006, 15.

Vaughan, D., and J. Isenberg (1984). Soil-structure interaction in explosive testing of model containments, *Nucl. Eng. Des.* **77,** no. 3, 229–250.

Wen, K.-L. (1994). Non-linear soil response in ground motions, *Earthquake Eng. Struct. Dynam.* **23,** no. 6, 599–608.

Wong, I. G., W. J. Silva, J. C. Pechmann, R. B. Darragh, and T. Yu (2011). Analyses of earthquake source, path, and site factors from ANSS data along the Wasatch Front, Utah, *Tech. Rept. 05HQGR0010, U.S. Geol. Surv.*, 86 pp.

Xu, J., J. Bielak, O. Ghattas, and J. Wang (2003). Three-dimensional nonlinear seismic ground motion modeling in basins, *Phys. Earth Planet. In.* **137,** no. 1–4, 81–95.

Zhang, B., and A. S. Papageorgiou (1996). Simulation of the response of the Marina District Basin, San Francisco, California, to the 1989 Loma Prieta earthquake, *Bull. Seismol. Soc. Am.* **86,** no. 5, 1382–1400.

Zhang, Y., J. P. Conte, Z. Yang, A. Elgamal, J. Bielak, and G. Acero (2008). Two-dimensional nonlinear earthquake response analysis of a bridge-foundation-ground system, *Earthquake Spectra* **24,** no. 2, 343–386.

R. Taborda
J. Bielak
D. Restrepo*
Computational Seismology Laboratory
Department of Civil and Environmental Engineering
Carnegie Mellon University
Pittsburgh, Pennsylvania 15213-3890
U. S. A.
rtaborda@cmu.edu

* Also at Departmento de Ingeniería Civil, Universidad EAFIT, Medellín, Colombia.